Journal of Biomechanics 46 (2013) 2701–2709

Contents lists available at ScienceDirect

Journal of Biomechanics

journal homepage: www.elsevier.com/locate/jbiomech
www.JBiomech.com

Finite element analysis and computed tomography based structural rigidity analysis of rat tibia with simulated lytic defects

John A. Rennick [a,c], Ara Nazarian [a], Vahid Entezari [a], James Kimbaris [a], Alan Tseng [a], Aidin Masoudi [a], Hamid Nayeb-Hashemi [c], Ashkan Vaziri [c], Brian D. Snyder [a,b,*]

[a] Center for Advanced Orthopaedic Studies, Beth Israel Deaconess Medical Center, Harvard Medical School, Boston, MA, USA
[b] Department of Orthopaedic Surgery, Children's Hospital, Harvard Medical School, Boston, MA, USA
[c] Department of Mechanical Engineering, Northeastern University, Boston, MA, USA

ARTICLE INFO

Article history:
Accepted 28 June 2013

Keywords:
Finite element analysis
Structural rigidity analysis
Metastatic disease
Lytic defect
Rat

ABSTRACT

Finite element analysis (FEA), CT based structural rigidity analysis (CTRA) and mechanical testing is performed to assess the compressive failure load of rat tibia with simulated lytic defects.

Twenty rat tibia were randomly assigned to four equal groups ($n=5$). Three of the groups included a simulated defect at various locations: anterior bone surface (Group 1), posterior bone surface (Group 2) and through bone defect (Group 3). The fourth group was a control group with no defect (Group 4). Microcomputed tomography was used to assess bone structural rigidity properties and to provide 3D model data for generation of the finite element models for each specimen.

Compressive failure load calculated using CT derived rigidity parameters (F_{CTRA}) was well correlated to failure load recorded in mechanical testing ($R^2=0.96$). The relationships between mechanical testing failure load and the axial rigidity ($R^2=0.61$), bending rigidity ($R^2=0.71$) and FEA calculated failure loads, considering bone as an elastic isotropic ($R^2=0.75$) and elastic transversely isotropic ($R^2=0.90$) are also well correlated. CTRA stress, calculated adjacent to the defect, were also shown to be well correlated with yield stresses calculated using the minimum density at the weakest cross section ($R^2=0.72$). No statistically significant relationship between apparent density and mechanical testing failure load was found ($P=0.37$).

In summary, the results of this study indicate that CTRA analysis of bone strength correlates well with both FEA and results obtained from compression experiments. In addition there exist a good correlation between structural rigidity parameters and experimental failure loads. In contrast, there was no correlation between average bone density and failure load.

© 2013 Elsevier Ltd. All rights reserved.

1. Introduction

One third to half of all cancers metastasize to bone (Coleman, 2006). In addition, post mortem examinations of breast and prostate cancer patients show a 70% incidence of metastatic bone disease (Mac Niocaill et al., 2011). Pathologic fracture of bones occurs when they can no longer support the loads to which they are subjected to (Snyder et al., 2009), and approximately 30–50% of bone metastases lead to fracture or produce symptoms severe enough to require treatment (Jawad and Scully, 2010).

Fracture risk is commonly quantified through assessment of the size, location and type of tumor as well as through analysis of a patient's bone mineral density (BMD). In addition to conventional radiographic techniques, the Mirels' criteria is also commonly used by clinicians in the assessment of fracture risk in patients with appendicular skeletal metastasis (Damron et al., 2003; Jawad and Scully, 2010; Mac Niocaill et al., 2011). Conventional plain radiographic techniques generally lack sensitivity with regard to fracture prediction and while Mirels' criteria has been shown to be sensitive, it is not specific (91% sensitive, 35% specific) (Damron et al., 2003; Mirels, 1989).

In contrast, Computed Tomography based Structural Rigidly Analysis (CTRA) can be used to monitor changes in bone geometry and material properties by assessing axial, bending and torsional rigidities. While CTRA has been used to assess fracture risk in studies of benign and metastastic musculoskeletal lesion in both humans and rats, it has not yet been the subject of extensive studies to compare its efficacy to advanced techniques such as finite element analysis (FEA) (Keyak et al., 2007; Keyak and Rossi, 2000; Mann et al., 2008; Orwoll et al., 2009; Pistoia et al., 2002; Schileo et al., 2008; Silva et al., 1998; Varghese et al., 2011, Hojjat et al., 2012).

Osteolytic metastasis is commonly associated with significant bone resorption and frequently results in fracture (Bunting et al., 1985; Van der Linden et al., 2004). Furthermore, lytic lesions are

* Correspondence to: Center for Advanced Orthopaedic Studies, Beth Israel Deaconess Medical Center, 330 Brookline Avenue, RN 115, Boston, MA 02215, USA. Tel.: +1 617 667 2940; fax: +1 617 667 7175.
E-mail address: brian.snyder@childrens.harvard.edu (B.D. Snyder).

0021-9290/$ - see front matter © 2013 Elsevier Ltd. All rights reserved.
http://dx.doi.org/10.1016/j.jbiomech.2013.06.024

typically more likely to result in fracture than blastic or mixed tumor cases (Mirels, 2003). As a result, a simulated lytic model was chosen to simulate this condition and used as a basis to compare the CTRA and FEA fracture risk methodologies. The simulated lytic defect model allows defect sites to be strictly controlled whereas the use of a metastatic tumor model seldom results in predictable defect sites in the diaphysis of the tibia, even with the use of the intracardiac injection method (Harms and Welch, 2003). In these cases, tumor cell clusters typically form in the proximal or distal regions (Phadke et al., 2006). In the current study, defect sites in the diaphysis of the tibia were favored as a means to compare the CTRA and FEA methodologies and hence a simulated lytic defect model was chosen.

Since CTRA is related to both bone mineral density distribution and structural variations, we hypothesize that CTRA can predict failure load as reliably as FEA in a simulated osteolytic rat bone defect model. CTRA assessments′ of bone failure load are presented by comparing linear regression coefficients of FEA and CTRA predicted failure loads versus those from mechanical testing. Investigations into correlations between experimental failure load and (1) apparent density, (2) curvature and (3) the axial and bending rigidities at the weakest cross section are also undertaken.

2. Materials and methods

2.1. Specimen preparation

This study was approved by Beth Israel Deaconess Medical Center Institutional Animal Care and Use Committee (IACUC). Twenty female Sprague Dawley rats (~15 weeks old, mass: 250–275 g) were obtained from Charles River laboratories (Charles River, Charlestown, MA, USA). One tibia, selected at random, was excised from each animal and all attached soft tissue removed. The attached fibula was removed prior to scanning with a high speed dremel hand saw. The locations of the simulated lytic defects were chosen to emulate common sites of in-vivo metastatic cancer. Lytic defects were simulated by drilling a hole at the desired location. All defects were made at the apex of the curved section of the bone using a 60 gauge (1.016 mm diameter) carbide drill bit under copious irrigation. The defect diameter was chosen to yield a circular hole diameter to specimen diameter ratio of approximately 25% (Hong et al., 2004). The primary goal of this study was to compare the CTRA and FEA methods of fracture risk assessment and hence a single well defined defect size was used in this study.

The tibiae were randomly assigned to four equal groups ($n=5$). Three of the groups included a simulated defect at various locations: anterior bone surface Group 1; posterior bone surface Group 2; and through bone defect Group 3. Group 4 was a control group with no defect. Typical specimens from each group are shown in Fig. 1.

2.2. Imaging and image analysis

Sequential transaxial images through the entire bone cross section were obtained using micro computed tomography (μCT40, Scanco Medical, AG, Brüttisellen, Switzerland). 30 μm isotropic voxel size was chosen in order to provide the required resolution for creating a solid model to perform the FEA analysis. This guaranteed that the scan resolution would be below the size of the edge length of the elements in the finite element models. The samples were scanned using an integration time of 250 ms and tube voltage and current of 70 kV and 114 μA respectively. Hydroxyapatite phantoms of known mineral density (0, 100, 200, 400 and 800 mg HA cm^{-3}), supplied by the manufacturer, were scanned to convert the x-ray attenuation coefficient (μ) to the bone mineral density (ρ_{EQUIV} [g cm^{-3}])

2.3. Structural rigidity analysis

Structural rigidity analysis is a technique used to predict fracture risk by defining the bones weakest cross section (Entezari et al., 2011; Hong et al., 2004; Snyder et al., 2006, 2009; Whealan et al., 2000). The axial rigidity (EA) and bending rigidity (EI) for each transaxial cross-sectional image through each tibia were calculated by summing the modulus-weighted area of each pixel comprising the bone section by its position relative to the centroid of the bone (Fig. 2).

The CTRA derived rigidity parameters can be combined with simple beam theory (Boresi and Schmidt, 2003) to define a CTRA based failure load (F_{CTRA}), which is defined as

$$F_{CTRA} = \frac{\varepsilon_{CRITICAL}\{\Sigma E_{ij}(\rho)da\}EI_{MAX}}{(EI_{MAX} + (\{\Sigma E_{ij}(\rho)da\}yD))} \quad (1)$$

where, $\varepsilon_{CRITICAL}$ is the critical bone strain at failure, E_{ij} and ρ are the local elastic modulus and density at the ijth location of the cross-section respectively, E (N mm^{-2}) is the average elastic modulus of the weakest cross section, da is the incremental cross sectional area (mm^2); I_{MAX} is the maximum moment of inertia (mm^4) at the weakest cross section; y is distance from geometric centroid to the bone surface where critical stress is present; and D is the distance from the eccentrically applied load to the geometric centroid at the weakest cross section. The maximum bending rigidity was used to calculate F_{CTRA} as the bending moment in mechanical testing and FEA simulations was applied around the minor principal axis (that which exhibited the maximum moment of inertia). The minimum bending rigidity (EI_{min}) was calculated and correlated to the mechanical testing failure load (F_{MECH}) to account for the "worst case" scenario.

In defining a CTRA based failure load (F_{CTRA}), the critical strain which identifies the onset of fracture ($\varepsilon_{CRITICAL}$) was set to 1.2% strain in compression, and 1% strain in tension (Hong et al., 2004; Keaveny et al., 1994; Pistoia et al., 2002; Snyder et al., 2009).

2.4. Mechanical testing

Specimens were tested using an Instron 8511 (Instron, Norwood, MA, USA) load frame under displacement control condition. Specimens were loaded to failure under uniaxial compressive at an axial strain rate of 0.01 s^{-1}. Both ends of the specimens were embedded in Polymethylmethacrylate (PMMA) to provide support.

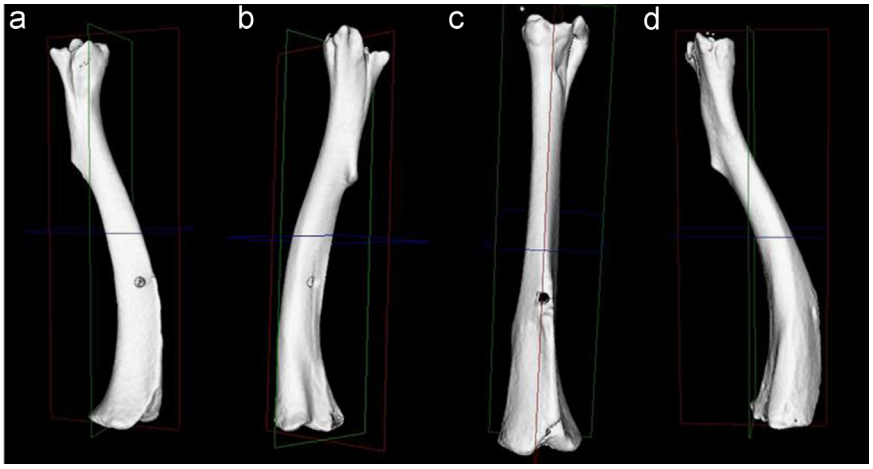

Fig. 1. Image of tibias, showing defect locations for the groups in the study: (a) Tibia from Group 1 (Anterior Defect); (b) Group 2 (Posterior Defect); (c) Group 3 (Through Hole Defect) and (d) Group 4 (Control). Sagittal (red), Coronal (Green) and Axial (Blue) Planes are shown. Fig. 2: Calculation of CTRA parameters for bone cross section. (For interpretation of the references to color in this figure legend, the reader is referred to the web version of this article.)

An ATI-Nano25 F/T 6-axis force transducer (ATI Industrial Automation, Apex, NC, USA) was used to measure loads during testing. Fig. 3 presents representative failed specimens.

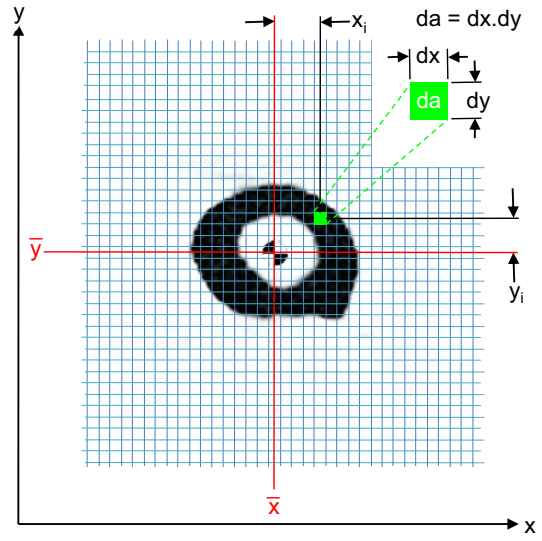

$$\bar{x} = \frac{\sum_{i=1}^{n} x_i E_i da}{\sum_{i=1}^{n} E_i da} \qquad \bar{y} = \frac{\sum_{i=1}^{n} y_i E_i da}{\sum_{i=1}^{n} E_i da} \qquad \text{(Equation 1)}$$

Fig. 2. Schematic diagram illustrating the pixel-based CTRA analysis technique to assess axial (EA) and bending (EI) rigidities presented here. Each grid element is intended to represent one pixel. The EA and EI equations have been presented here, where s represents bone density, x_i and y_i represent the distance of each pixel along the y- and x-axes respectively, da represents the area of each pixel, E_i represents Young's modulus of elasticity (defined as the ratio of compressive strength to strain in the linear region). Each pixel is filtered through a bone density threshold and converted to material modulus (E) and using empirically derived relationships for rat bone as a function of bone density. Relative distance between pixels is determined by calibration of imaging modality. Modulus weighted neutral axis and centroid (Eq. (1) in Fig. 2) are determined based on the coordinates of the ith pixel, its modulus(E_i), area (da) and total number of pixels in the bone cross-section (n). Axial rigidity (Eq. (2)in Fig. 2) is the sum of the products of each pixel's elastic modulus (E_i) and pixel area (da). Bending rigidity about the y-axis (Eq. (2) in Fig. 2) is the sum of the products of the elastic modulus (E_i), square of the distance ith pixel to the neutral axis (y) and the pixel area (da).

2.5. Finite element analysis

The details of the finite element models developed in this research are presented in Supplementary data. Abaqus CAE v6.10 (SIMULIA, Providence, RI) was used to perform all finite element simulations. Boundary conditions consisted of an analytic rigid plate tied to the nodes on the distal surface of the tibia via a rigid body interaction defined in ABAQUS. An axial displacement of 2 mm was then applied to this plate at an axial strain rate of 0.01 s^{-1}. This boundary condition was chosen to match the mechanical testing conditions.

FEA failure load (F_{FEA}) was calculated for each of the four material models used and was calculated by recording the percentage of the bone volume strained to 1% in tension and 1.2% in compression at two distinct time points during the analysis. The critical strain values were chosen based on yield strain values for bone published in the literature (Keaveny et al., 1994). Principal strains were monitored for each increment of the finite element simulation, as compressive load was increased, and failure was defined when two percent of the bone volume reached the principal strain limit of 1.2% in compression and 1% in tension (Keaveny et al., 1994). A typical maximum and minimum principal strain distribution is shown in Fig. 4. The associated sum of the reaction forces at the fixed nodes was also calculated for each of these time points. A plot of the reaction forces versus the percentage of bone volume above the strain limit was created for each specimen. The failure criterion, which was based on 2% of the bone volume exceeding the strain limits, was applied to each curve and linear interpolation used to estimate the FEA fracture load. This failure criterion was established based on the best correlation with the experimental data.

In defining this criterion various percentile bone volumes (0.5, 1, 2, 4 and 8%) were trialed. The strain limits of 1.2% and 1% in compression and tension and bone volume fraction of 2% exceeding this strain range resulted in relations more closely aligned to the experimental data and to $y=x$ line ($P=0.9638$) than other criterion.

In addition to the principal strain limit criterion highlighted, the Coulomb Mohr criterion was also trialed as a predictor of estimated fracture load and compared to the principal strain criterion used in the bulk of this study. The results are shown in Table 3. The Coulomb Mohr criterion is defined as (Shigley and Mischke, 1988)

$$\frac{\sigma_{1i}}{S_{ti}} \geq 1 \quad (\sigma_{1i} > 0,\ \sigma_{2i} > 0,\ \sigma_{3i} > 0,\ \sigma_{1i} > \sigma_{2i} > \sigma_{3i})$$

$$\frac{\sigma_{1i}}{S_{ci}} \geq 1 \quad (|\sigma_{1i}| > |\sigma_{2i}| > |\sigma_{3i}| > 0,\ \sigma_{1i} < 0,\ \sigma_{2i} < 0,\ \ldots \sigma_{3i} < 0)$$

$$\frac{\sigma_{1i}}{S_{ti}} - \frac{\sigma_{3i}}{S_{ci}} \geq 1 \quad (\sigma_{1i} > \sigma_{2i} > 0,\ \sigma_{3i} < 0) \qquad (2)$$

where σ_{1i},σ_{2i}, and σ_{3i} are principal stresses. S_{ti} and S_{ci} are the tensile and compressive failure stresses respectively defined based on the element level density using previously derived relations (Keyak and Rossi, 2000). Large deformation and the small strain theory was used in all simulations performed in ABAQUS (van Rietbergen et al., 1995).

2.6. Statistical analysis

Linear regression analysis was used to assess how well both FEA and CTRA analyses can be used to predict failure load when compared to mechanical testing.

Fig. 3. Three representative images showing fractured tibiae following mechanical testing.

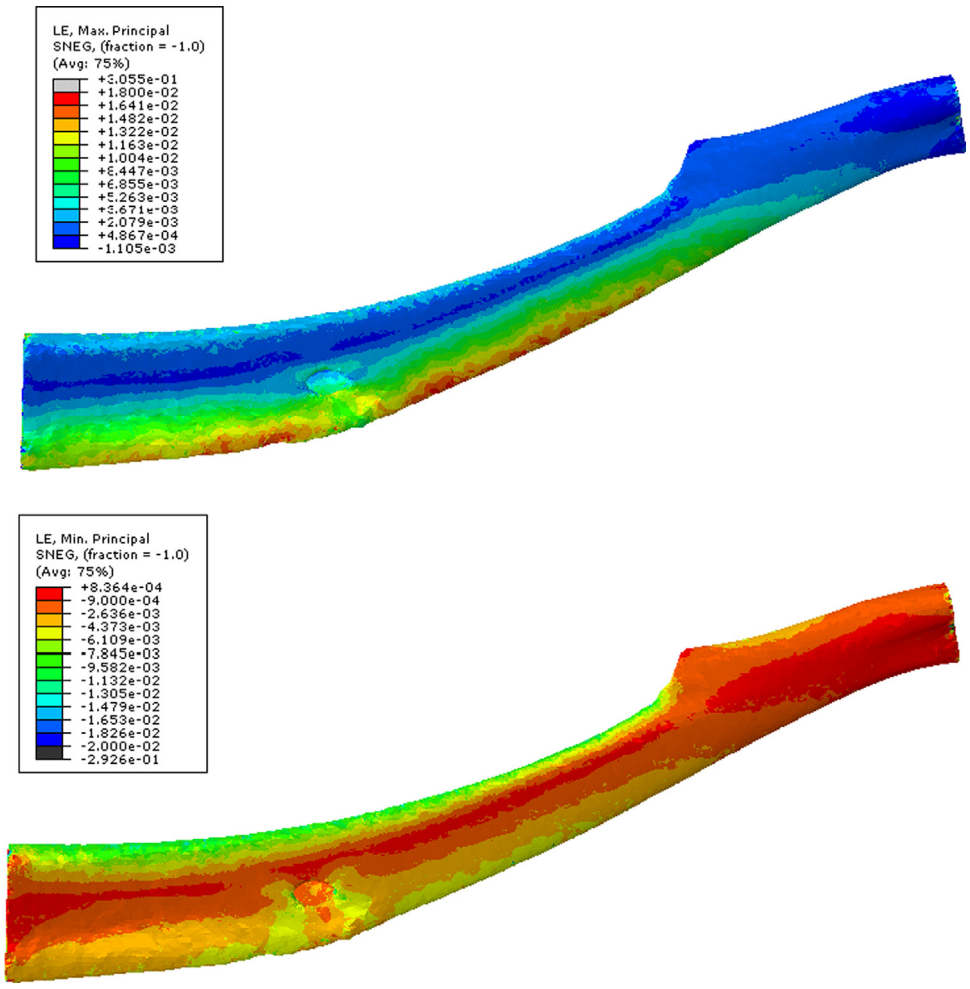

Fig. 4. (a) Maximum (tensile) and (b) Minimum (compressive) principal strains present at failure in representative finite element models.

Investigations into statistical differences between the resulting regression lines and the slope and intercept of the $y=x$ line were also undertaken.

Regressions for mechanical testing failure load against FEA and CTRA derived loads were investigated further using Fisher's z transformation test to analyze for statistical differences between the various models. Linear regression was also undertaken to correlate mechanical testing failure load to apparent density, radius of curvature and structural rigidity parameters EA, EI_{MIN} and EI_{MAX}. The resulting coefficients of determination (R^2) were used as the criterion by which to compare each of the regression models. Statistical analysis was performed using the SPSS software package (Version 18.0, SPSS Inc., Chicago, IL, USA). Two tailed values of $P<0.05$ were considered statistically significant.

3. Results

All results are shown in Tables 1–3. All specimens including a simulated lytic defect fractured through that defect, as shown in Fig. 3. Control specimens failed across the weakest cross section identified via CT scans. FEA results showed that the maximum stress developed at the defect site for all specimens in groups two (posterior defect) and three (through hole defect), but for no specimens within group one (anterior defect). Interestingly, the maximum bending rigidity was higher for the specimens in this group, but this did not result in an increased failure load prediction. In all FEA simulations performed a greater bone volume reached the critical limit in tension than that in compression, suggesting that specimens in all groups failed on the anterior (tensile) surface, which matched with the failure mechanisms observed in mechanical testing performed.

Very high correlation between mechanical testing (F_{MECH}) and CTRA calculated (F_{CTRA}) failure load is observed. Fig. 5a shows the relation between F_{CTRA} and F_{MECH} ($R^2=0.96$, $P<0.001$). Fig. 5a also shows that the slope of the regression curve did not deviate from the $y=x$ line [$F_{MECH}=1.0662F_{CTRA}-4.8006$] ($P=0.96$). In addition, the y intercept was also shown to be not different from zero ($P=0.54$).

Furthermore, results in Table 3 show a good correlation between FEA and mechanical testing loads for the various material models used. A linear elastic, isotropic model accounted for 75% of the variation in failure load ($R^2=0.75$, $P<0.001$) (Table 3). Utilizing a linear elastic, perfectly plastic post yield model improved the resulting correlation slightly ($R^2=0.77$, $P<0.001$) (Table 3). In both cases, the FEA predicted failure load was higher for three specimens within Group 4 which reduced the resulting linear regression coefficient when compared to the CTRA derived failure load regression curve (see Table 3). In the CTRA analysis performed, the loads were estimated more accurately for those three specimens within the Group 4, which resulted in a higher regression coefficient ($R^2=0.96$, $P<0.001$). The failure criteria used in the current study in the FEA simulations has therefore been shown to be less able to predict failure in healthy bone (Group 4 specimens), though was capable of accurately predicting failure load in tumor burdened bone (Groups 1–3). In addition to the elastic, isotropic material model assumption, an elastic transversely isotropic material model was also used. The use of the elastic transversely isotropic material model improved the resulting correlation coefficient for both the elastic transversely isotropic ($R^2=0.90$, $P<0.001$) (Fig. 5b) and

Table 1
The parameters reported in the table are F_{MECH}: the mechanical testing failure load, ρ_{APP}: the apparent density of the weakest cross section, ρ_{EQUIV}: the equivalent bone density of the weakest cross section, E_{CTRA}: modulus of elasticity derived using previously developed relations (Cory et al. 2010), K_{MECH}: the axial stress divided by the axial strain from mechanical testing, F_{CTRA}: the CTRA based failure load, F_{FEA}: the FEA estimated failure load using isotropic, linear elastic material model and ε_{YIELD}: the estimated yield strain obtained using CTRA parameters.

		F_{MECH}	ρ_{APP}	ρ_{EQUIV}	E_{CTRA}	K_{MECH}	F_{CTRA}	F_{FEA}	ε_{YIELD}
		N	g cm^{-3}	g cm^{-3}	MPa	MPa	N	N	mm/mm
Group 1	Median	164.40	2.509	1.656	20723	21000	153.63	98.88	0.010288
	Min	134.13	2.483	1.639	20324	18000	130.37	92.83	0.010073
	Max	166.60	2.578	1.702	21807	21286	165.39	107.33	0.010701
Group 2	Median	144.60	2.496	1.648	20536	18625	139.50	104.16	0.010289
	Min	121.38	2.461	1.624	19986	16600	121.39	93.15	0.009856
	Max	158.38	2.672	1.764	23317	19400	154.23	107.33	0.010681
Group 3	Median	112.87	2.554	1.685	21424	18250	109.58	82.83	0.009800
	Min	93.82	2.396	1.581	19019	14500	95.74	66.55	0.008229
	Max	170.33	2.701	1.782	23785	19400	159.86	109.70	0.010364
Group 4	Median	134.17	2.608	1.721	22291	16699	129.52	97.38	0.011478
	Min	127.89	2.505	1.653	20660	16400	127.76	81.91	0.008739
	Max	140.47	2.770	1.828	24948	19182	134.78	100.81	0.013369

Table 2
The parameters reported in the table are σ_{CTRA}: stress calculated using CTRA, σ_{YIELD}: density dependent yield strength calculated using relations from Cory et al. 2010, σ_{FEA}: The stress in FEA at same location as CTRA calculated stress, and $\sigma_{FEA\text{-}MAX}$: the maximum stress in the FEA model. Area: the area of the weakest cross section, EA: the axial rigidity of the weakest cross section, EI_{MIN}: the minimum bending rigidity of the weakest cross section, EI_{MAX}: the maximum bending rigidity of the weakest cross section.

		σ_{CTRA}	σ_{YIELD}	σ_{FEA}	$\sigma_{FEA\text{-}MAX}$	Area	EA	EI_{MIN}	EI_{MAX}
		MPa	MPa	MPa	MPa	mm^2	N	N mm^2	N mm^2
Group 1	Median	209.11	241.34	240.99	319.16	4.96	107635	77483	181438
	Min	208.74	237.27	181.13	264.62	4.33	87903	70871	160157
	Max	233.36	252.38	265.83	505.60	5.19	108252	79205	202421
Group 2	Median	212.94	239.42	216.89	481.40	4.50	92658	77909	128396
	Min	206.91	233.80	205.99	443.51	4.00	88198	61957	105883
	Max	233.16	267.64	239.05	645.50	5.32	111725	86050	144285
Group 3	Median	213.35	248.49	211.03	567.75	4.02	79098	68493	110549
	Min	185.84	223.84	194.32	409.40	3.37	69331	63371	85820
	Max	220.67	272.34	247.85	644.30	4.18	99396	102868	170916
Group 4	Median	265.68	257.25	215.48	314.85	4.51	99887	53890	123551
	Min	180.55	240.70	161.94	216.67	4.18	86299	41034	93649
	Max	312.76	283.99	318.06	429.30	4.72	105276	91216	157453

Table 3
Parametric analysis of material models and failure theories. The equations for each of the linear regressions are presented in this table, along with the corresponding correlation coefficient (R^2) and P statistic comparing each regression with the $y=x$ line. The P values for the slope and y-intercept are shown separately.

Material model	Failure criteria	Equation	R^2	P	
				Slope	y-inter
Isotropic, elastic	Prinicipal strain (1% ten, 1.2% comp)	$0.993F_{FEA}+12.369$	0.75	0.964	0.538
	Coulomb Mohr	$1.9447F_{FEA}+0.6398$	0.80	0.312	0.173
	CTRA	$1.0662F_{FEA}-4.820$	*0.96*	0.286	0.571
	Prinicipal strain (0.8% ten, 1% comp)	$1.6274F_{FEA}-16.493$	0.75	0.020	0.509
Isotropic, elastic, perfectly plastic	Prinicipal strain (1% ten, 1.2% comp)	$0.8601F_{FEA}+30.629$	0.77	0.272	0.074
	Coulomb Mohr	–	–	0.011	0.000
Transversely isotropic	Prinicipal strain (1% ten, 1.2% comp)	$0.8183F_{FEA}+39.114$	*0.90*	0.039	0.004
	Coulomb Mohr	$1.5925F_{FEA}+20.591$	0.67	0.199	0.561
Transversely isotropic, perfectly plastic	Prinicipal strain (1% ten, 1.2% comp)	$0.8149F_{FEA}+37.021$	0.87	0.022	0.001
	Coulomb Mohr	–	–	<0.0001	<0.0001

elastic-perfectly plastic transversely isotropic models ($R^2=0.87$, $P<0.001$). Interestingly, the elastic-perfectly plastic transversely isotropic model predicted a higher failure load for a single specimen in Group 4 (Control), which in the elastic transversely isotropic model, it predicted to be lower than observed in mechanical testing. This difference between the predicted failure load for this specimen in the two models accounts for the reduction in the correlation coefficient observed for the elastic-perfectly plastic transversely isotropic model. Comparing the strain criteria used in the F_{CTRA} model and the results obtained from the various Coulomb–Mohr theories, these findings indicate that there is better correlation between local failure prediction from the F_{CTRA} model as supported by the reported P values. Further analysis to evaluate collagen fiber orientation with respect to crack propagation direction {Peterlik, 2006 #15752} at the edges of lytic defects will help elucidate the role of bone toughness on the failure model.

The mechanical testing showed that all specimens failed by brittle fracture. Accordingly, accounting for plasticity results in minor

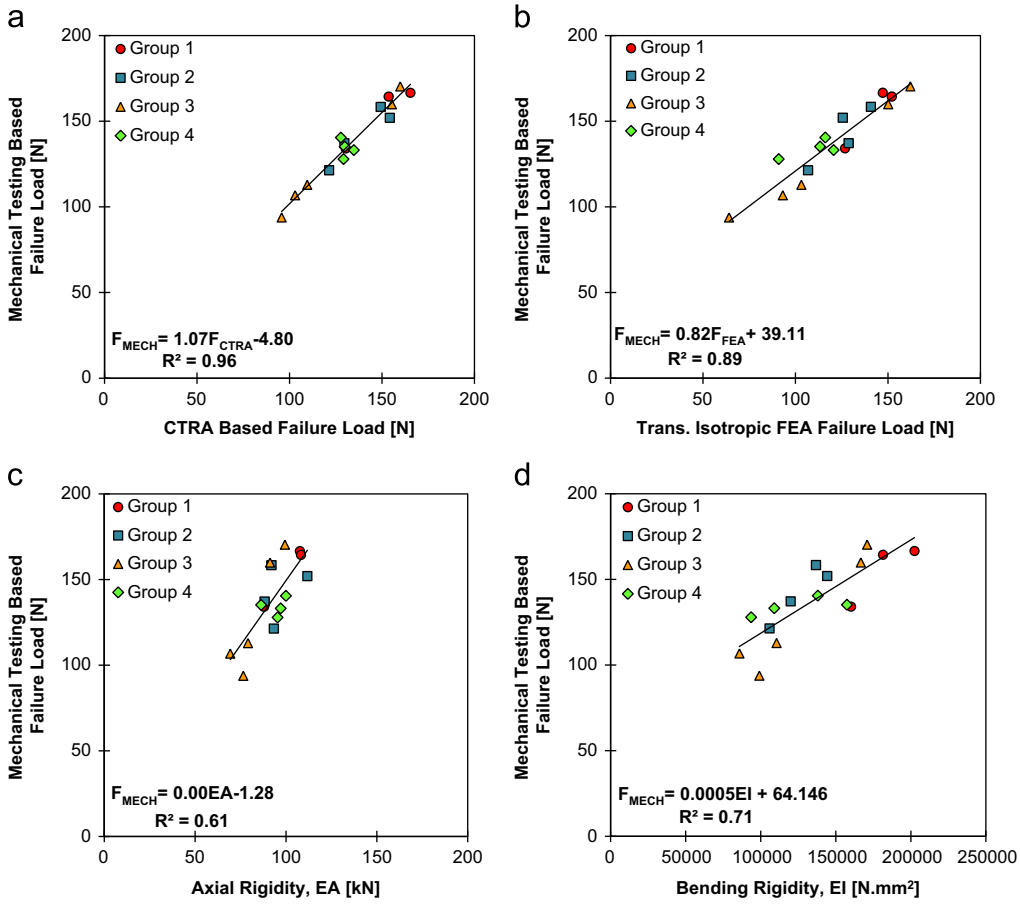

Fig. 5. Linear Regression of (a) CTRA vs Mech Failure Load; (b) transversely Isotopic FEA vs Mech Failure Load; (c) EA vs Mech Failure Load; and (d) EI_{max} vs Mech Failure Load.

changes to the final regression correlation coefficients. In addition to using strain limits of 1.2% in compression and 1% in tension, a lower strain threshold limit (1% in compression, 0.8% in tension) was trialed for the linear elastic, isotropic model to investigate the effects this had on results. Whilst the regression coefficient remained unchanged ($R^2=0.75$), the FEA failure loads were calculated to be 1.6 times lower than mechanical testing failure loads [$F_{MECH}=1.6274F_{FEA}-16.493$] (Table 3). Statistically, the slope was not significantly different when compared to the $y=x$ line ($P=0.19$) nor was the y intercept significantly different than zero ($P=0.51$) for this criteria. However, use of the higher principal strain limit allowed for higher failure load predictions in FEA models. As a result correlations were closer to the $y=x$ line ($P=0.96$). The equations and statistical analysis for each of the regression curves is shown in Table 3. Correlations between FEA and CTRA calculated failure loads are slightly reduced ($R^2=0.71$, $P<0.001$) but remain significant when using the lower strain failure criteria. The results obtained using CTRA analysis also confirm that bone generally fails at a constant strain which is independent of modulus (Keaveny et al., 1994).

The Coulomb Mohr criterion performed well in predicting failure for the isotropic, linear elastic model ($R^2=0.80$, $P<0.001$). It also provided reasonable correlation for the elastic transversely isotropic material model ($R^2=0.67$, $P<0.001$). The Coulomb Mohr failure criteria was less satisfactory in predicting failure for the elastic perfectly plastic material models for both the elastic-perfectly plastic isotropic ($P=0.52$) and the elastic-perfectly plastic transversely isotropic ($P=0.60$) models. In both cases, the regression coefficient was poor, as the criterion was unable to predict failure in specimens where plasticity effects were considered.

Fig. 5c and d shows the correlations between mechanical testing failure loads and EA ($R^2=0.61$, $P<0.001$) and EI_{MAX} ($R^2=0.71$, $P<0.001$). The result indicates that the bending rigidity of the weakest cross section accounts for 71% of the experimentally obtained failure load, and that EA accounts for only 60% of the failure load. Similarly, EI_{MIN} accounted for 71% of the variation ($R^2=0.71$, $P<0.001$). Neither parameter fully accounts for the failure load due to the presence of both bending and axial stresses, though correlations are strong. Moreover, neither apparent density ($P=0.37$) nor the radius of curvature at the weakest cross section ($P=0.26$) exhibited a strong correlation with the experimentally obtained failure load, F_{MECH}.

We have also shown good correlation between CTRA calculated stress and the density dependent yield stress, using the density at the weakest cross section ($R^2=0.72$, $P<0.001$), as shown in Table 2.

4. Discussion

This study investigated the correlation between FEA, CTRA and mechanical testing based failure loads in a rat bone model of simulated osteolytic defects.

In the finite element modeling performed in this study, the elastic modulus of each element was related to the density of each element which allowed the bone heterogeneity to be explicitly modeled. Four simulations were undertaken for each specimen. In the first, a linear elastic isotropic material assumption was made. In the second, elastic transversely isotropic material properties

were assigned relative to the centroidal axis of each tibia. In the third and fourth simulations performed, the elastic isotropic and elastic transversely isotropic cases included perfectly plastic behavior post yielding. This model was adopted to investigate the effects of possible plastic deformations adjacent to the defect (The term perfectly plastic deformation in this paper simply refers to the material that get additional strain without additional stress. This can be considered as the collapse of cellular structure after its elastic deformation). Mechanical testing results showed that all specimens failed via brittle fracture and hence the yield and ultimate stresses were coincident.

In the elastic-perfectly plastic simulation, the yield stress of each element was defined based on relations previously derived to relate yield stress to element level density (Cory et al., 2010). The FEA simulations incorporating plasticity effects highlighted that many specimens failed via brittle fracture, with no plastic deformation, the predicted failure load for the two models was unchanged. Interestingly, the principal strain criterion was able to accurately predict the failure load for both the elastic-perfectly plastic isotropic and transversely isotropic, whilst the Coulomb Mohr criterion, which is most suited to the study of brittle failure mechanisms (Gdoutos, 2005), did not result in a good correlation with the experimental data (Table 3).

The model used here considered four cases of lytic lesion locations, namely through hole defect, anterior defect, posterior defect and a no defect control group. The location of each defect created was strictly controlled. All specimens had a defect diameter to specimen diameter ratio of approximately 25%. Furthermore, the loading mode was an eccentric axial compressive load.

The simulated lytic defect used in this study was a circular hole with possible sharp edges, a condition seldom seen in biological scenarios, where tumors with poorly defined borders or indistinct margination are typical (Zelazny et al., 1997). It has been shown when the edges of the defect are blurred, lower stress values are typically observed (Kourtis et al., 2008, Weber et al., 2007). However, in the current study it is possible that stress concentrations arising from the adjacent sharp edges did not adversely affect the load predictive capabilities of the two failure (fracture) criteria studied here. We believe the crack tips of any possibly formed cracks get blunted by the presence of microcavities in the bone during mechanical loading, thus reducing stress concentration. Furthermore, our experimental data were in good agreement with the FEA results, which did not consider any cracks. Thus, all material and failure models trialed were not sensitive to any erroneous stress concentrations arising as a result of the sharp edges present. Additional work is required to provide additional insight into the topic. However, we concede that the perfect circle shape of the defect does not correspond to metastatic lesions observed in patients. This study is considered a stepping stone to help conduct similar studies in animal models of skeletal metastasis with actual lytic lesions.

Keyak and co-authors have studied and assessed the performance of several failure theories for the CT/FE models of the proximal femur (Keyak and Rossi, 2000). In a study of human cadaveric proximal femur specimens with and without metastatic lesions, a strong linear relationship ($R^2=0.83$) between predicted and actual strength was shown (Keyak et al., 2005). It has been shown that even a defect as small as 3.0 mm can significantly increase the risk of fracture (Keyak et al., 2007). Keyak et al. also showed that CT/FE models can be used to predict the strength of shaft of femur without or with metastases and they may be applicable for predicting the risk of pathologic femoral shaft fractures (Keyak et al., 2005). These studies are congruent with our study and findings. Simulated lytic models have also been used to study variations in hip strength associated with variations in defect size and anatomic location (Kaneko et al., 2008).

In addition to the material and failure models presented here, the Tsai Wu and super ellipsoid criterion have also been applied by others where anisotropic material models are used (Bayraktar et al., 2004; Keaveny et al., 1999). Furthermore, other authors have also studied the effects of utilizing the distortion energy and Hoffman failure theories with good results (Keyak and Rossi, 2000).

The primary goal of this study was to compare the efficacy of the CTRA and FEA methods for a variety of material models and failure criterion for the case of a curved beam such as the tibia. The Computed Tomography based Structural Rigidity Analysis (CTRA) methods presented here assumes small displacement and composite beam theory with the structural parameters obtained from spiral transaxial CT images. Enhanced results could be achieved by analyzing cross sections normal to the neutral axis when seeking area and moment of inertia parameters for use in the CTRA load calculation. Additionally, curved beam theory (Boresi and Schmidt, 2003; Mourtada et al., 1996) could also be used to enhance the calculated CTRA stresses and the associated failure loads, where the defect site was in a region of relatively high curvature. However, as we have shown in this study, when the radius of curvature is large, straight beam theory often gives reasonable results.

We have compared the use of CTRA and FEA analysis in defining the fracture risk associated with eccentric axial compressive loading in a simulated osteolytic rat tibia defect model. CTRA has been shown to be as good as the more sophisticated FEA in calculating the failure load for this load case. Furthermore, CTRA calculations were performed in a significantly shorter computation time (greater than 2 h for FEA and less than 30 min for CTRA). Whilst the use of patient specific finite element models is perhaps not yet feasible in a clinical setting due to time constraints, the use of CTRA methods has been shown to be a viable technique in assessing clinical fracture risk. The CTRA method has been shown to greatly enhance fracture assessments compared to conventional radiographic techniques alone in prospected in-vivo human study (Snyder et al., 2006).

Despite the simplifying assumptions made in this study, the CTRA method was able to accurately predict the failure loads in a curved, heterogeneous, anisotropic, elliptically shaped cross section bone undergoing large deformations. The results of this study show CTRA to be an extremely useful method for fracture risk assessment in an osteolytic rat model, where both axial and bending stresses are present. Previously, our group has shown that CTRA can be used to accurately calculate failure load in the torsional loading mode for rat femurs with simulated lytic defects of various size (Entezari et al., 2011) and predicting failure in tension, four point bending and torsion of cancelled bone samples harvested from whale spines (Hong et al., 2004).

5. Conflicts of interest

There are no conflicts of interest to report.

Acknowledgments

Professor Sinan Muftu, Northeastern University, is gratefully acknowledged for providing access to the software required to generate the finite element models. In addition, the authors also wish to thank the reviewers who provided detailed and helpful comments to aid in improving the manuscript content.

Appendix A. Supplementary data

Finite element model creation: Mimics Software v13.1 (Materialise, Leuven, Belgium) was used to construct a 3D solid model of

Fig. 6. Finite Element Mesh as presented in a specimen.

each tibia using sequential transaxial CT images, as shown in Fig. 6. The resulting 3D solid model was smoothed in order to simplify the model and remove any voids or sharp edges present on the surface.

Quadratic ten node tetrahedral elements with a mean edge length of ~0.5 mm were used. The mesh density was selected based on mesh convergence studies undertaken; each model consisted of approximately 90,000–120,000 elements. The mesh was refined adjacent to the defect, with a mean edge length of ~0.15 mm in this region. The mesh density was gradually decreased as the distance from the defect increased. A higher mesh density was used adjacent to the defect to better map the stress and strain distribution in this region.

In the finite element model, elastic moduli were assigned at the element level based on the bone density (Cory et al. 2010). One hundred distinct material properties were assigned to each finite element model in order to allow the effects of bone heterogeneity to be incorporated into the model. This resulted in a modulus distribution in the complete finite element model from approximately 2 GPa to 30 GPa. The mean longitudinal modulus of elasticity assigned to all finite element models was 21.37 ± 1.45 GPa, which was approximately equal to published values for the elastic modulus of cortical bone (Cory et al. 2010; Bayraktar et al., 2004). Four material models were considered in the finite element analyses. The four models considered were (A) linear elastic, isotropic; (B) linear elastic –perfectly plastic isotropic; (C) linear elastic transversely isotropic; and (D) linear elastic-perfectly plastic transversely isotropic. The mean transverse elastic modulus in the elastic transversely isotropic model was 15.32 ± 1.11 GPa and the mean longitudinal and transverse shear moduli were 8.30 ± 0.60 GPa and 5.89 ± 0.49 GPa respectively. The yield stress was assigned to each element based on the element level density using previously derived relationships (Cory et al. 2010). The mean yield stress assigned was 340.24 ± 29.09 MPa. Poisson's ratio for isotropic and transversely isotropic models in the longitudinal direction was set to 0.3 and was chosen based on values previously used in the literature (Pistoia et al., 2002; Bayraktar et al., 2004). Poisson ratios for other directions in the transversely isotropic model were obtained based on the relations between elastic constants in the transversely isotropic materials.

References

Bayraktar, H.H., Gupta, A., Kwon, R.Y., Papadopoulos, P., Keaveny, T.M., 2004. The modified super-ellipsoid yield criterion for human trabecular bone. Journal of Biomechanical Engineering 126, 677–684.

Boresi, A.P., Schmidt, R.J., 2003. Advanced Mechanics of Materials. John Wiley & Sons, Inc., NY.

Bunting, R., Lamont-Havers, W., Schweon, D., Kliman, A., 1985. Pathologic fracture risk in rehabilitation of patients with bony metastases. Clinical orthopaedics and Related Research, 222–227.

Coleman, R.E., 2006. Clinical features of metastatic bone disease and risk of skeletal morbidity. Clinical Cancer Research 12, 6243s-6249s.

Cory, E., Nazarian, A., Entezari, V., Vartanians, V., Muller, R., Snyder, B.D., 2010. Compressive axial mechanical properties of rat bone as functions of bone volume fraction, apparent density and micro-ct based mineral density. Journal of Biomechanics 43, 953–960.

Damron, T.A., Morgan, H., Prakash, D., Grant, W., Aronowitz, J., Heiner, J., 2003. Critical evaluation of mirels' rating system for impending pathologic fractures. Clinical Orthopaedics and Related Research 415, S201–S207.

Entezari, V., Basto, P.A., Vartanians, V., Zurakowski, D., Snyder, B.D., Nazarian, A., 2011. Non-invasive assessment of failure torque in rat bones with simulated lytic lesions using computed tomography based structural rigidity analysis. Journal of Biomechanics 44, 552–556.

Gdoutos, E.E., 2005. Fracture Mechanics: An Introduction. Springer, NY.

Harms, J.F., Welch, D.R., 2003. MDA-MB-435 human breast carcinoma metastasis to bone. Clinical and Experimental Metastasis 20, 327–334.

Hojjat, S.P., Beek, M., Akens, M.K., Whyne, C.M., 2012. Can mico-imaging based analysis methods quantify structural integrity of rat Vertebrae with and without metastic involvment? Journal of Biomechanics 45, 2342–2348.

Hong, J., Cabe, G.D., Tedrow, J.R., Hipp, J.A., Snyder, B.D., 2004. Failure of trabecular bone with simulated lytic defects can be predicted non-invasively by structural analysis. Journal of Orthopedic Research: Official Publication of the Orthopedic Research Society 22, 479–486.

Jawad, M.U., Scully, S.P., 2010. In brief: classifications in brief: Mirels' classification: metastatic disease in long bones and impending pathologic fracture. Clinical Orthopaedics and Related Research 468, 2825–2827.

Kaneko, T.S., Skinner, H.B., Keyak, J.H., 2008. Lytic lesions in the femoral neck: Importance of location and evaluation of a novel minimally invasive repair technique. Journal of Orthopedic Research: Official Publication of the Orthopedic Research Society 26, 1127–1132.

Keaveny, T.M., Wachtel, E.F., Ford, C.M., Hayes, W.C., 1994. Differences between the tensile and compressive strengths of bovine tibial trabecular bone depend on modulus. Journal of Biomechanics 27, 1137–1146.

Keaveny, T.M., Wachtel, E.F., Zadesky, S.P., Arramon, Y.P., 1999. Application of the Tsai-Wu quadratic multiaxial failure criterion to bovine trabecular bone. Journal of Biomechanical Engineering 121, 99–107.
Keyak, J.H., Kaneko, T.S., Skinner, H.B., Hoang, B.H., 2007. The effect of simulated metastatic lytic lesions on proximal femoral strength. Clinical Orthopaedics and Related Research 459, 139–145.
Keyak, J.H., Kaneko, T.S., Tehranzadeh, J., Skinner, H.B., 2005. Predicting proximal femoral strength using structural engineering models. Clinical Orthopaedics and Related Research, 219–228.
Keyak, J.H., Rossi, S.A., 2000. Prediction of femoral fracture load using finite element models: an examination of stress- and strain-based failure theories. Journal of Biomechanics 33, 209–214.
Kourtis, L.C., Carter, D.R., Kesari, H., Beaupre, G.S., 2008. A new software tool (VA-BATTS) to calculate bending, axial, torsional and transverse shear stresses within bone cross sections having inhomogeneous material properties. Computer Methods in Biomechanics and Biomedical Engineering 11, 463–476.
Mac Niocaill, R.F., Quinlan, J.F., Stapleton, R.D., Hurson, B., Dudeney, S., O′Toole, G.C., 2011. Inter- and intra-observer variability associated with the use of the Mirels′ scoring system for metastatic bone lesions. International Orthopaedics 35, 83–86.
Mann, K.A., Lee, J., Arrington, S.A., Damron, T.A., Allen, M.J., 2008. Predicting distal femur bone strength in a murine model of tumor osteolysis. Clinical Orthopaedics and Related Research 466, 1271–1278.
Mirels, H., 1989. Metastatic disease in long bones. A proposed scoring system for diagnosing impending pathologic fractures. Clinical Orthopaedics and Related Research, 256–264.
Mirels, H., 2003. Metastatic disease in long bones: A proposed scoring system for diagnosing impending pathologic fractures. Clinical Orthopaedics and Related Research, S4–13.
Mourtada, F.A., Beck, T.J., Hauser, D.L., Ruff, C.B., Bao, G., 1996. Curved beam model of the proximal femur for estimating stress using dual-energy X-ray absorptiometry derived structural geometry. Journal of Orthopedic Research: Official Publication of the Orthopedic Research Society 14, 483–492.
Orwoll, E.S., Marshall, L.M., Nielson, C.M., Cummings, S.R., Lapidus, J., Cauley, J.A., Ensrud, K., Lane, N., Hoffmann, P.R., Kopperdahl, D.L., Keaveny, T.M., 2009. Finite element analysis of the proximal femur and hip fracture risk in older men. Journal of Bone and Mineral Research 24, 475–483.
Phadke, P.A., Mercer, R.R., Harms, J.F., Jia, Y., Frost, A.R., Jewell, J.L., Bussard, K.M., Nelson, S., Moore, C., Kappes, J.C., Gay, C.V., Mastro, A.M., Welch, D.R., 2006. Kinetics of metastatic breast cancer cell trafficking in bone. Clinical Cancer Research 12, 1431–1440.
Pistoia, W., van Rietbergen, B., Lochmuller, E.M., Lill, C.A., Eckstein, F., Ruegsegger, P., 2002. Estimation of distal radius failure load with micro-finite element analysis models based on three-dimensional peripheral quantitative computed tomography images. Bone 30, 842–848.
Schileo, E., Taddei, F., Cristofolini, L., Viceconti, M., 2008. Subject-specific finite element models implementing a maximum principal strain criterion are able to estimate failure risk and fracture location on human femurs tested in vitro. Journal of Biomechanics 41, 356–367.
Shigley, J., Mischke, C., 1988. Mechanical Engineering Design, 5th edition McGraw Hill, NY.
Silva, M.J., Keaveny, T.M., Hayes, W.C., 1998. Computed tomography-based finite element analysis predicts failure loads and fracture patterns for vertebral sections. Journal of Orthopedic Research: Official Publication of the Orthopedic Research Society 16, 300–308.
Snyder, B.D., Cordio, M.A., Nazarian, A., Kwak, S.D., Chang, D.J., Entezari, V., Zurakowski, D., Parker, L.M., 2009. Noninvasive prediction of fracture risk in patients with metastatic cancer to the spine. Clinical Cancer Research 15, 7676–7683.
Snyder, B.D., Hauser-Kara, D.A., Hipp, J.A., Zurakowski, D., Hecht, A.C., Gebhardt, M. C., 2006. Predicting fracture through benign skeletal lesions with quantitative computed tomography. Journal of Bone and Joint Surgery, (American) 88, 55–70.
Van der Linden, Y.M., Dijkstra, P.D., Kroon, H.M., Lok, J.J., Noordijk, E.M., Leer, J.W., Marijnen, C.A., 2004. Comparative analysis of risk factors for pathological fracture with femoral metastases. Journal of Bone and Joint Surgery, British 86, 566–573.
van Rietbergen, B., Weinans, H., Huiskes, R., Odgaard, A., 1995. A new method to determine trabecular bone elastic properties and loading using micromechanical finite-element models. Journal of Biomechanics 28, 69–81.
Varghese, B., Short, D., Penmetsa, R., Goswami, T., Hangartner, T., 2011. Computed-tomography-based finite-element models of long bones can accurately capture strain response to bending and torsion. Journal of Biomechanics 44, 1374–1379.
Weber, M.H., Sharp, J.C., Latta, P., Hassard, T.H., Orr, F.W., 2007. Early detection and quantification of murine melanoma bone metastases with magnetic resonance imaging. Skeletal Radiology 36, 659–666.
Whealan, K.M., Kwak, S.D., Tedrow, J.R., Inoue, K., Snyder, B.D., 2000. Noninvasive imaging predicts failure load of the spine with simulated osteolytic defects. Journal of Bone and Joint Surgery, American volume 82, 1240–1251.
Zelazny, A., Reinus, W.R., Wilson, A.J., 1997. Quantitative analysis of the plain radiographic appearance of Ewing′s sarcoma of bone. Investigative Radiology 32, 59–65.